"Metal-free" electrocatalysis

Molina Garcia, Miguel; Rees, Neil

[Link to publication on Research at Birmingham portal](#)

"Metal-free" electrocatalysis: Quaternary-doped graphene and the alkaline oxygen reduction reaction

Miguel A. Molina-García, Neil V. Rees*

Centre for Doctoral Training in Fuel Cells and their Fuels, School of Chemical Engineering, University of Birmingham, Edgbaston, Birmingham, B15 2TT, UK

ARTICLE INFO

ABSTRACT

We report the first investigation into a quaternary-doped graphene catalyst material for the oxygen reduction reaction (ORR) under alkaline conditions. The material was synthesized via direct pyrolysis of graphene oxide (GO) with boron, nitrogen, phosphorus and sulfur precursors. The resulting BNPS-Gr catalyst was thoroughly characterized and its composition found via XPS to be 6.4% (B), 6.1% (N), 2.6% (P) and 0.5% (S), while HR-TEM imaging shows a few-layered graphene structure. Electrochemical investigations into the catalytic activity towards the ORR show improved performance of the quaternary-doped graphene with the effective number of electrons transferred being ca. 3.7, compared to single-doped graphenes (2.9–3.2) and significantly lower peroxide production. This demonstrates BNPS-Gr to be a promising alternative to current Pt-group catalysts for the ORR, especially in methanol-fuelled fuel cells, where the presence of methanol in the cathode side from the fuel crossover is shown not to affect the performance of the quaternary-doped graphene catalyst.

1. Introduction

Graphene is increasingly finding application within catalysis due to its intrinsic properties [1–3], and in particular its catalytic activity towards the oxygen reduction reaction (ORR) has generated significant interest [4,5]. The ORR is a persistent challenge for researchers of energy applications (e.g. fuel cells, metal-air batteries) due to its slow kinetics [6,7]. Pristine graphene has demonstrated a limited ORR performance due to its zero band gap, which weakens the catalytic activity [8,9]. A promising strategy to make graphene more catalytically active towards the ORR is doping the graphene structure with *p*-block heteroatoms, such as nitrogen [10–16], boron [17–21], phosphorus [22–24] or sulfur [25–28], since the inclusion of dopant atoms in the 2D graphene structure can modify the electroneutrality of the sp^2 carbon lattice and create sites for O_2 adsorption [29]. It has been suggested that the formation of carbon active sites induced by the heteroatoms alters the binding energy of the molecule of O_2, favouring the dissociation of the O=O bond [30]. Several methods have been proposed for the doping of graphene with heteroatoms, including chemical vapour deposition (CVD), ball milling, bottom-up synthesis, thermal annealing, wet chemical method, plasma treatment with heteroatom atmosphere or arc-discharge [31]. Among these methods, CVD is one of the most widespread, nevertheless it is a relatively complex process whose application entails the use of hazardous precursors and gases, contamination by transition metal reagents, high cost of the process and

a low yield [32]. Most of these problems can be overcome using a thermal annealing treatment of a mixture of precursors under an inert atmosphere for the synthesis of the catalyst [33].

According to the literature, the different heteroatoms play specific roles inside the carbon structure. For example, the electron-deficient B atoms act as active sites for O_2 adsorption and favour the O–O bond cleavage [34]. The N atoms produce active catalytic sites, via inducing an asymmetrical spin and charge density changes (such as C$^+$ creation), thus improving the ORR performance [35]. The electron-donating properties of P induce defects in the graphene layer through the creation of P$^+$ charge sites and increase the electron delocalization [36]. The catalytic active sites in S-doped graphene are the C atoms located at the zigzag edges or close to the SO_2 adsorbed species that enhance the spin density of carbon [25]. In spite of promising results reported for the single-doped graphene catalysts, their catalytic activity is still far away from that reported for traditional Pt-group catalysts [23,28,37]. Consequently, several authors have synthesized dual [38–43] and ternary-doped [44–49] graphene catalysts, demonstrating that the different heteroatoms incorporated into the graphene structure act synergistically, improving the catalytic activity with respect to the single-doped graphenes. In addition, a higher variability in the electronegativity of the doping heteroatoms could induce an asymmetrical spin and charge density redistribution, thus improving the ORR performance [35].

To the best of our knowledge, there are no papers reporting if this

---

behaviour can be extended to metal-free quaternary-doped graphene. Since the interaction of different heteroatom-carbon species has demonstrated to act synergistically for dual and ternary-doped graphenes, we believe that the synthesis of a quaternary-doped graphene may open a range of further possible catalyst materials. Previously, an innovative quaternary-doped graphene with N, P, S and Fe, synthesized from direct pyrolysis of *Shewanella oneidensis* bacteria, has been developed and studied, showing a catalytic current density even comparable to commercial Pt/C [50]. Nevertheless, the presence of metals in the catalyst has been related to several disadvantages, namely poor stability, low selectivity, higher cost than metal-free catalysts and a negative environmental impact [51]. In this work, we present a novel metal-free quaternary-doped graphene synthesized via an easy method of GO thermal annealing in presence of B, N, P and S dopant precursors under an inert atmosphere. This catalyst is physically characterized using high-resolution transmission electron microscopy (HR-TEM), scanning TEM (STEM), energy-dispersive X-ray spectroscopy (EDX), X-ray diffraction (XRD), Raman spectroscopy, Brunauer–Emmett–Teller (BET) analysis and X-ray photoelectron spectroscopy (XPS), and its electrochemical ORR performance is compared with the equivalent single-doped catalysts.

2. Experimental

2.1. Catalyst preparation

All the catalysts were prepared via a thermal annealing of a mixture formed by GO (Nanoinnova, ref.: GO.M.10.29-1) and the precursors of the different doping agents. The precursors were boric acid, melamine, dibenzyl disulfide (all Sigma Aldrich, $\geq 98\%$), and orthophosphoric acid (Fisher Scientific, 86.75%). For the single-doped catalysts 100 mg of GO were mixed with 500 mg of precursor (except 100 mg in the case of dibenzyl disulfide) in 30 mL of ultrapure water (resistivity ≥ 18.2 MΩ cm, milli-Q Millipore). For the quaternary-doped catalyst the composition of the mixture was 100 mg of GO, 200 mg of boric acid, 300 mg of melamine, 500 mg of phosphoric acid and 100 mg of benzyl disulphide in 30 mL of ultrapure water. The ink was sonicated (Ultrawave, 50 Hz) for 1 h and then stirred for 15 h, before being concentrated by centrifugation at 20,000 rpm for 10 min at room temperature (Centrifuge Sigma 3K-30 refrigerated). The resulting mixture was placed on an alumina crucible and pyrolised in a quartz tubular furnace (Vecstan Ltd. F400414) at 900 °C for 2 h, heating rate of 5 °C min^{-1} from room temperature, under 50 mL min^{-1} N$_2$ atmosphere (BOC gases, O$_2$ free, 99.998% purity). Finally, the sample was left to cool at room temperature under N$_2$ atmosphere before being collected and weighed.

2.2. Physical characterization

The different catalysts were imaged by a transmission electron microscopy (TEM) using a JEOL 2100F at 200 kV, equipped with a FEG source and a Gatan Orius CCD camera in order to obtain images with 0.025 nm pixel resolution. The EDS spectra were taken on a Tecnai F20 FEG (S)TEM operating at 200 kV, equipped with an Oxford Instruments X-Ma SDD EDX system. The TEM and STEM-EDS samples were prepared by drying a 10 μL droplet of catalyst aqueous suspension on a Cu grid. The XRD measurements were obtained using a PANalytican Empyrean Pro X-ray powder diffractometer with a not monochromated Cu X-ray source. Raman spectra were recorded using a Raman Microscope Renishaw inVia system with an excitation laser wavelength of 532 nm. The specific surface areas and porous structures of the quaternary-doped catalyst were measured with a Micromeritics TriStar II Plus adsorption instrument by physical adsorption-desorption of N$_2$ at 77 K. X-ray photoelectron spectroscopy (XPS) spectra were obtained at the National EPSRC XPS Users' Service (NEXUS) at Newcastle University using a Thermo Scientific K-Alpha XPS instrument with a monochromatic Al Kα X-ray source.

2.3. Electrochemical characterization

For the ex-situ characterisation of the catalysts rotating ring-disk voltammetry was performed using a Metrohm AutoLAB PGSTAT128N potentiostat connected to a rotator (Pine Instrument Inc.) in a Faraday cage. The reference electrode was an Ag/AgCl (sat. KCl) electrode (ALS Inc. RE-1CP, E^0 = +0.197 V vs SHE) and the counter electrode was a homemade Pt mesh. The RRDE (E7R9 Series, Pine Instruments Inc., USA) consisted of a GC disk (5.61 mm diameter) and a Pt ring with an area of 0.1866 cm^2, with a collection efficiency of 37%. Prior to each experiment the RRDE was thoroughly polished with consecutive alumina slurries of 1, 0.3 and 0.05 μm (Buehler, ITW Company) and then sonicated to remove any impurities. The catalyst inks were prepared dispersing 5 mg of the required catalyst in 0.2 mL of isopropyl alcohol (VWR Chemicals), 0.78 mL of ultrapure water and 0.02 mL of 10 wt% Nafion (Ion Power Inc.), obtaining a resulting catalyst concentration of 5 mg mL^{-1}. This mixture was sonicated for 1 h and then a 15 μL aliquot was pipetted onto the GC disk to give a catalyst loading of 0.3 mg cm^{-2}. The droplet was left to dry at room temperature for 30 min at 500 rpm as described in literature [52] in order to get an uniform layer.

The RRDE was then immersed in the O$_2$-saturated (BOC gases, N5, 99.999% purity) 0.1 M KOH (Sigma-Aldrich, 99.99%) alkaline solution and cycled between +0.4 and −1.0 V at 100 mV s^{-1} until a stable response was observed. Linear sweep voltammograms (LSV) were then recorded at 10 mV s^{-1} between +0.4 and −1.0 V at rotation speeds from 400 to 2400 rpm. The Pt ring voltage was fixed at +0.5 V to ensure complete HO$_2^-$ decomposition [53]. Methanol tolerance was tested by current-time chronoamperometry at −0.5 V (vs. Ag/AgCl) and 1600 rpm rotation rate for 300 s. 4.36 mL of methanol (Fisher Chemical, 99.99%) was added after 60 s into the alkaline solution (175 mL) to give a 0.6 M methanol concentration. All measurements were carried out at 293 ± 2 K.

3. Results and discussion

The single and quaternary-doped graphene catalysts (namely BNPS-Gr, B-Gr, N-Gr, P-Gr and S-Gr) were prepared as described above. The nanostructure of BNPS-Gr was investigated by HR-TEM imaging. Fig. 1a and b show the characteristic wrinkled veil-like structure of the graphene sheets, with a randomly stacked and overlapped distribution of layers, and local areas which show agglomeration and disorder of the 2D structure. Fig. 1c also reflects the presence of graphene nanosheets albeit with non-uniform layer thickness, demonstrating variability in the number of graphene sheets. This feature is shown in greater detail in Fig. 1d where the individual graphene nanosheets can be seen with theoretical thickness of 0.35 nm [54]. The inset clearly shows a 6-layer stack, although there are regions with a higher number of graphene sheets. The incorporation of B, N, P and S into the graphene structure is clearly visualized from the STEM-EDX images reflected in Fig. 2, where it can be observed that a great amount of oxide groups still remain after the thermal treatment. In addition, it can be seen that B and N are incorporated into the catalyst in a bigger extent than P and S, results that will be confirmed by XPS measurements later.

Next, the surface area of the quaternary doped-graphene catalyst was examined by N$_2$ adsorption-desorption isotherms at 77 K (Fig. 3a) and calculated according to the BET method. A type-II isotherm is observed, with the intermediate flat region between the values of P/P$_0$ = 0.1 and 0.7 corresponding to a monolayer formation characteristic of microporous materials [55]. The calculated specific BET surface area was 78.6 ± 0.3 m^2 g^{-1}, which is higher or similar to other reported doped-graphene catalysts, such as single N-doped graphene [56] or ternary (N, P, B)-doped nanoporous carbons [48]. The pore size distribution is shown in Fig. 3b. Using the Barrett–Joyner–Halenda (BJH) method, the average pore diameter is calculated to be 6.2 nm, whereas
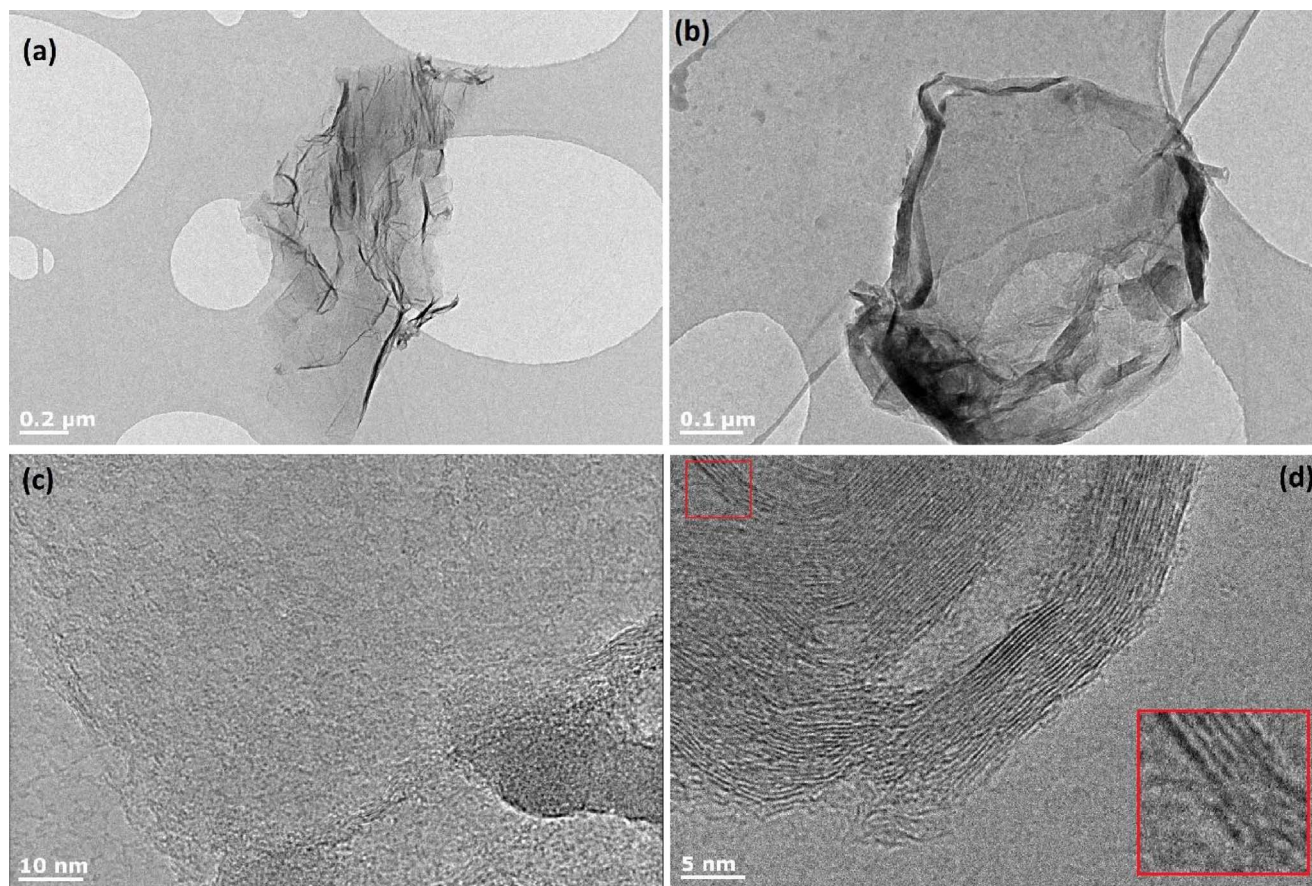
Fig. 1. (a) (b) Low-resolution and (c) (d) high-resolution TEM images of the quaternary-doped graphene catalyst. Inset: Higher resolution HR-TEM image showing a 6-layer graphene stack.

the corresponding pore volume is determined as $0.12 \, cm^3 \, g^{-1}$. These results suggest that the BNPS-Gr has a mesoporous structure, with the pore size ranging between 2 and 50 nm characteristic of mesoporous materials [57].

XRD and Raman spectroscopy measurements were carried out to characterize the structure of the different catalysts. The XRD patterns (Fig. 4a) show a distinctive diffraction peak at $2\theta = 11.6°$ for the GO precursor corresponding to a (002) index related to an interlayer space of 0.79 nm. This feature points to the presence of oxide groups allocated in the basal space between layers [58]. After pyrolysis, this peak disappears and a new broader peak arises at around $2\theta = 26.5°$, which is in agreement with the intense narrow peak observed in pristine graphene at 26.6° associated to a basal space between consecutive layers of 0.34 nm [56]. It should be noted that the values of 2θ corresponding to the C(002) peak are in inverse correlation to the distance between consecutive graphene layers [59]. Fig. 4a shows that the value of 2θ for the C(002) peak is 26.7° for B-Gr and N-Gr, whereas that for P-Gr, S-Gr and the quaternary BNPS-Gr this value is around 26.3°. Since B and N have a smaller atomic radius than P and S, the interlayer space is decreased (thus 2θ bigger) in B-Gr and N-Gr with respect to P-Gr and S-Gr. For graphene catalysts simultaneously doped with different heteroatoms, the value of 2θ will be determined by the larger atoms present in their structure. Hence, the 2θ value corresponding to the C(002) peak of BNPS-Gr is the same of that observed in P-Gr and S-Gr. Beside this, the width and intensity of the C(002) peak in the doped graphene catalysts compared to exfoliated graphene indicate that the restoration of graphene structure was only partial. The conclusion of these results is that annealing partially recovers the crystal structure of pristine graphene due to the reduction of the oxide groups present in the GO precursor. The faint peak appearing at around 43° corresponds to (100) reflections

in the carbon phase [24].

The Raman spectra were obtained under ambient conditions and show the characteristic peaks corresponding to the D and G bands at 1340 and $1580 \, cm^{-1}$, respectively (see Fig. 4b). The D band is attributed to the presence of defects or distortion of the 2D graphene lattice, whereas the G band is produced by stretching of the sp^2 bonds between carbon atoms and it is commonly associated to the degree of graphitization [20]. The ratio of D and G bands (I_D/I_G) is a good indicator of the degree of structural disorder of a material and values are indicated in Fig. 4b for all the catalysts. The I_D/I_G ratio is lower for B-Gr and N-Gr (ca. 1.05) with respect to P-Gr and S-Gr (ca. 1.35). This suggests that the integrity of the graphene structure is dependent on the size of the doping atoms, rather than the amount of doping species incorporated into the graphene layers. The quaternary-doped catalyst shows an I_D/I_G ratio of 1.24, which reflects the incorporation of the different heteroatoms (Table 1). It is observed that the values of I_D/I_G ratio in the Raman spectra keep an inverse correlation with the intensity of the C(002) peaks reflected in the XRD graph, noting that both features are closely related to defects present on the graphene structure [59]. Raman spectra can also provide information about the mean crystallite size (L_a) of the different doped-graphenes via the Tuinstra–Koenig (TK) equation [60]:

$$\frac{I_D}{I_G} = \frac{C(\lambda)}{L_a} \tag{1}$$

being C(532) $\sim 49.56 \, Å$ [61] (nevertheless, it should be noted that the TK method has been questioned in the literature [62], where it is stated not being valid over all ranges of L_a and wavelengths). The values of L_a are shown in Table 1. It can be seen that the mean crystallite size of the different doped-graphene catalysts has been reduced with respect to GO due to the thermal treatment applied and the incorporation of the
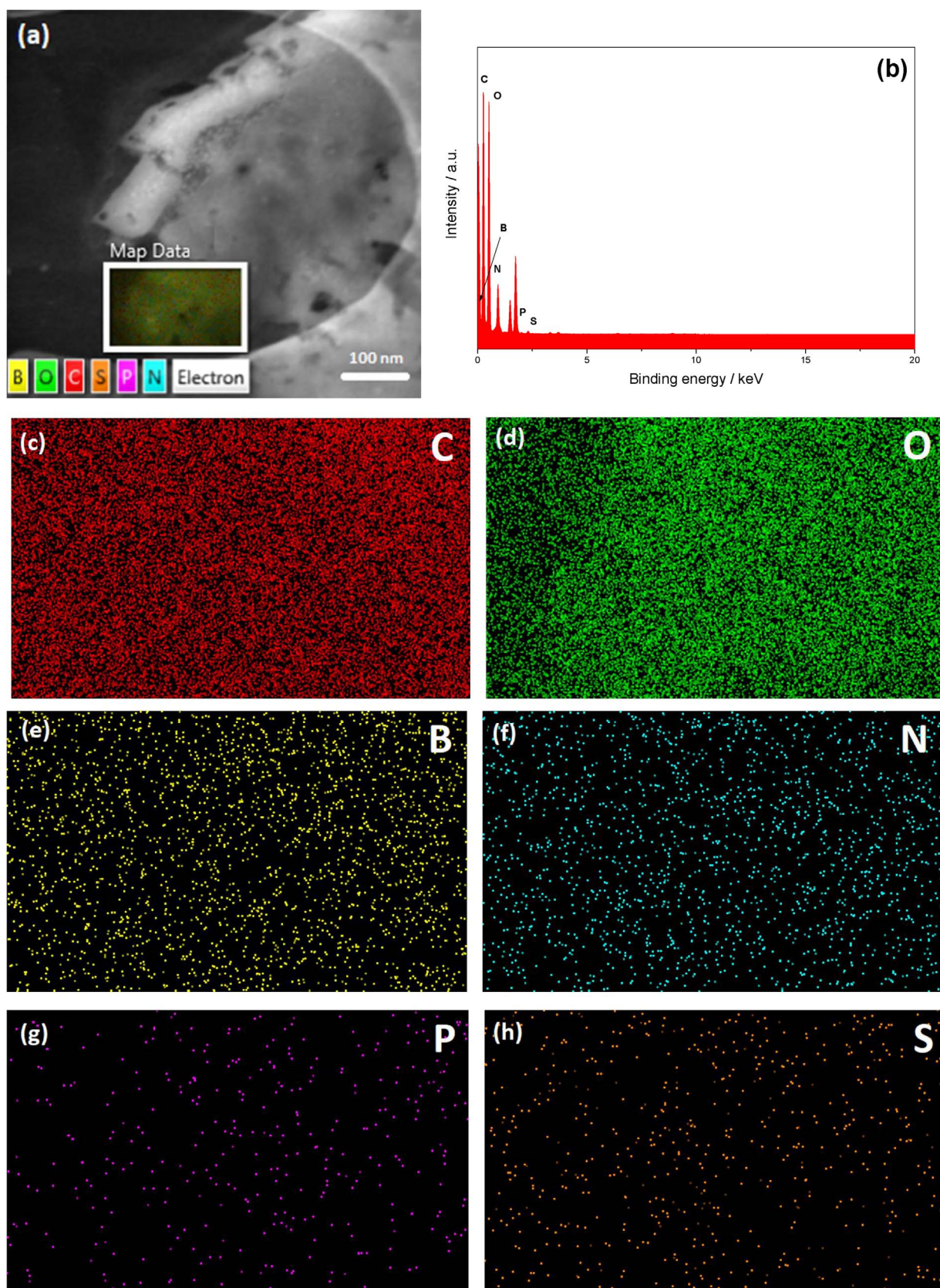
Fig. 2. (a) STEM image and (b) EDX spectra of BNPS-Gr, (c–h) with the corresponding C, O, B, N, P and S elemental mappings, respectively.
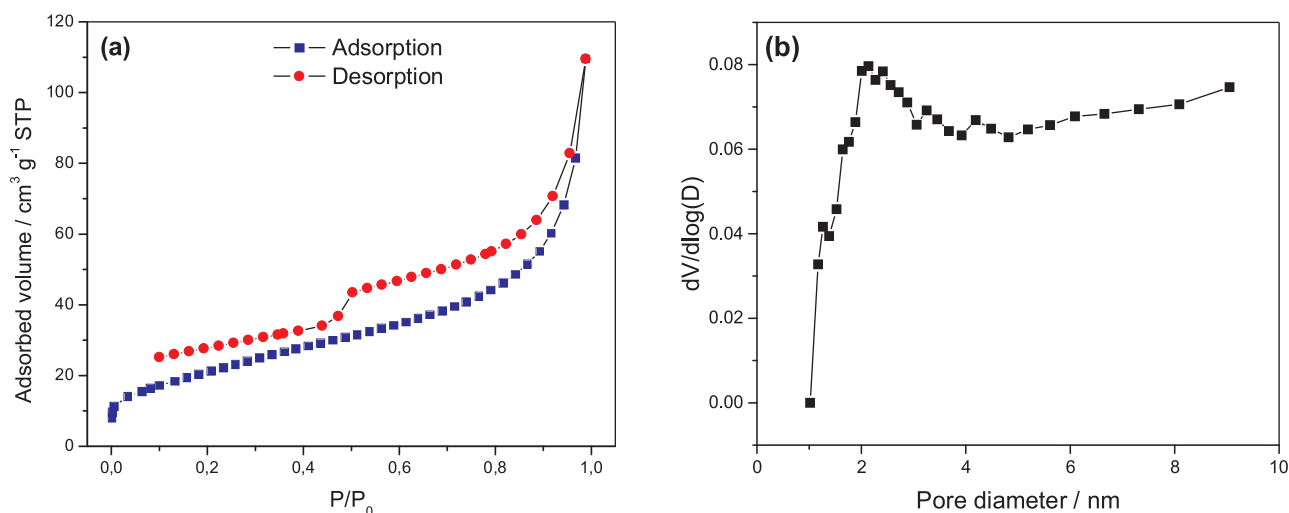
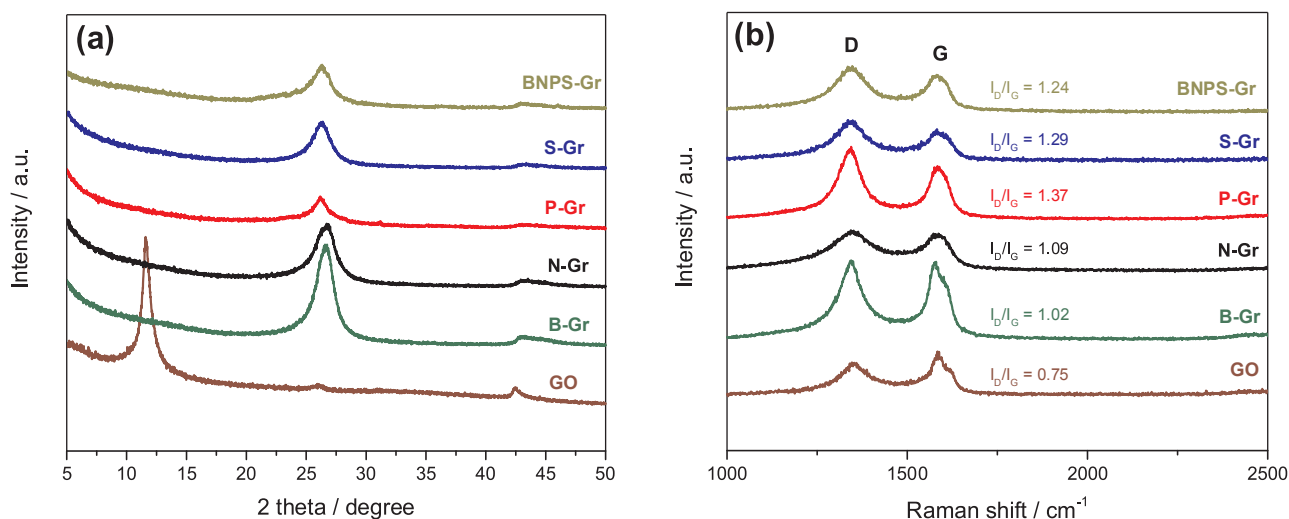**Fig. 3.** (a) Nitrogen adsorption/desorption isotherms and (b) pore size distribution of the BNPS-Gr.

Fig. 4. (a) XRD patterns of all catalysts, including the GO precursor. (b) Raman spectra of the prepared catalysts using an excitation laser wavelength of 532 nm. The calculated I_D/I_G values are also presented.

Table 1
I_D/I_G ratios and mean crystallite size (L_a) of the different catalysts obtained from the Raman spectra.

Catalyst	GO	B-Gr	N-Gr	P-Gr	S-Gr	BNPS-Gr
I_D/I_G	0.75	1.02	1.09	1.37	1.29	1.24
L_a (Å)	66.1	48.6	45.5	36.2	38.4	40.0

different heteroatoms into the graphene structure [61]. This is in agreement with the higher I_D band observed in doped graphenes with respect to GO, as a consequence of the hexagonal symmetry distortion of graphene due to the incorporation of heteroatoms [59]. The mean crystallite size of BNPS-Gr is shown to be an average value of those reported for the single-doped graphenes, demonstrating that all the individual heteroatoms have been effectively incorporated into the graphene.

To investigate the chemical composition of the synthesized catalysts, XPS measurements were performed (Fig. 5) and show the typical peaks for C, O, B, N, P and S, confirming that the doping precursors are effectively incorporated into the graphene structure. The composition of the different catalysts was calculated from the area under the peaks (Table 2), being these results in good agreement with the images obtained from the STEM-EDX analysis shown in Fig. 2. It is noted that the
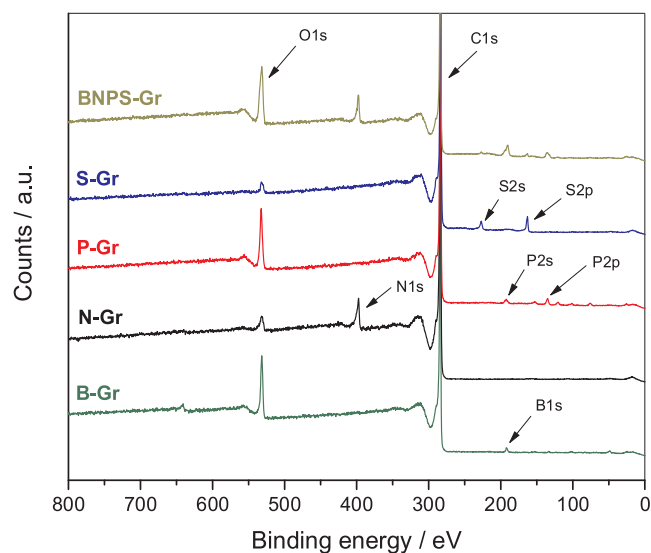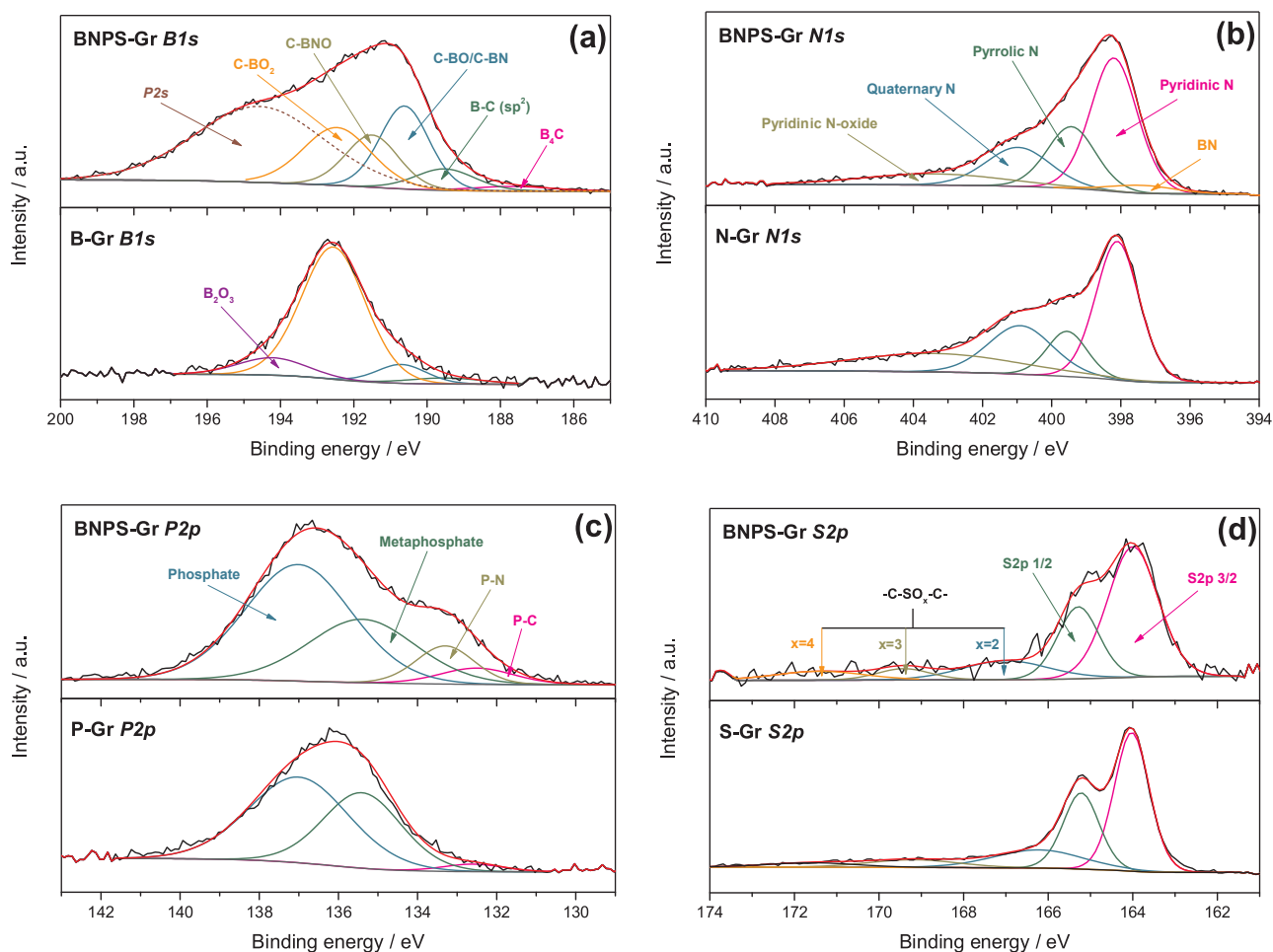

Fig. 5. Survey XPS spectra of the prepared catalysts, showing the peaks corresponding to the dopants.

Table 2
Catalyst compositions (calculated from XPS measurements) with their corresponding errors.

Catalyst (atom %)	C	O	B	N	P	S
GO	68.0 ± 0.2	32.0 ± 0.2				
B-Gr	88.1 ± 0.1	9.1 ± 0.1	2.8 ± 0.1			
N-Gr	91.8 ± 0.5	2.6 ± 0.6		5.6 ± 0.5		
P-Gr	88.8 ± 0.3	9.4 ± 0.3			1.8 ± 0.2	
S-Gr	95.8 ± 0.1	1.6 ± 0.2				2.6 ± 0.1
BNPS-Gr	72.6 ± 1.2	11.8 ± 0.5	6.4 ± 0.6	6.1 ± 0.1	2.6 ± 0.2	0.5 ± 0.1

Fig. 6. Corel level XPS spectra of (a) B1s, (b) N1s, (c) P2p and (d) S2p of the quaternary-doped graphene (top) and the corresponding single-doped catalyst (bottom).

broader peak appearing at around 195 eV in the quaternary-doped catalyst is consistent with a combination of both the B1s and the P2s moieties, therefore the P2s contribution was calculated from the P2p peak and subtracted to the overall area in order to obtain the content of B in BNPS-Gr. A high variability in the O content can also be observed, suggesting that the mechanism of dopant incorporation into the graphene 2D structure is different depending on the identity of the dopant species.

To gather insight into the mechanism of doping and the nature of the bonds formed during the annealing treatment, XPS spectra were recorded for the different species and are displayed in Fig. 6. The deconvoluted B1s spectrum (Fig. 6a) for the B-Gr catalyst is fitted to four peaks at 189.5, 190.6, 192.5 and 194.1 eV, attributable to B-C (sp^2), C-BO, C-BO$_2$ and B$_2$O$_3$, respectively [21,63]. The same peak in BNPS-Gr, however, is clearly distorted due to the presence of the other species. From the left, the distortion is due to the overlap of the P2s peak with the B1s moiety, presumably due to the incorporation of the P dopant into the structure [64]. Therefore, the P2s contribution had to be

subtracted (its area was calculated to be 44% of the overall area, from the relation P2s/P2p in P-Gr showed in Fig. 5) before proceeding with the analysis of the B species. The B1s peak is also shifted to the right due to BN species arisen at 191.4 eV (C-BNO) and 190.6 eV (C-BN), together with the contribution of B$_4$C at 187.9 eV [63]. The deconvolution of the N1s spectrum (Fig. 6b) generates four N species, namely pyridinic N (398.1 eV), pyrrolic N (399.4 eV), quaternary N (400.8 eV) and pyridinic N-oxide (403.4 eV) [65]. In this case, the small differences between N-Gr and BNPS-Gr are influenced by pyrrolic N and B-N species (397.4 eV) in the quaternary-doped catalyst [66]. The P2p peak observed in P-Gr (Fig. 6c) can be mainly deconvoluted into two oxidised species, namely metaphosphates (135.2 eV) and phosphorus at higher oxidation levels (137.2 eV) [67], phosphates which remain unaltered from the phosphoric acid precursor [68], and a very small contribution of the P−C bond (132.7 eV). A distortion at the right of this peak appears for BNPS-Gr due to the incorporation of P−N species (133.4 eV) and an increased amount of P−C bonds [69]. Finally, the S2p feature (Fig. 6d) is virtually identical for S-Gr and BNPS-Gr, with 75% of
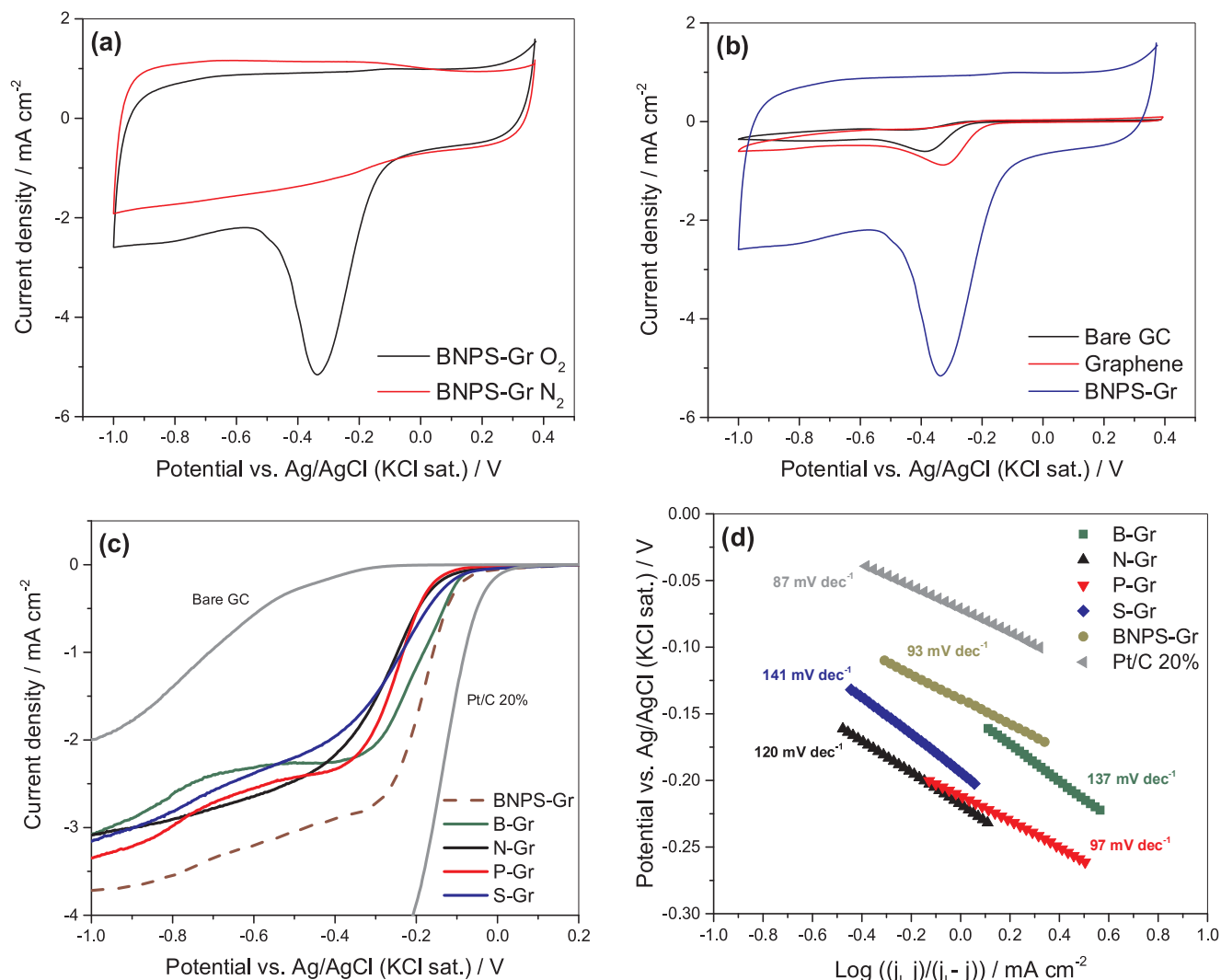
Fig. 7. (a) Cyclic voltammograms (CV) of BNPS-Gr catalyst in N_2 and O_2-saturated 0.1 M KOH solution, measured at 100 mV s^{-1}. (b) CVs of Bare GC, Graphene and BNPS-Gr. (c) LSV measurements of the catalysts in O_2-saturated 0.1 M KOH solution, measured at 10 mV s^{-1} and 1600 rpm. A commercial Pt/C 20% and Bare GC electrode are also shown for comparison. (d) Tafel plots corresponding to the data shown in (c).

−C−S−C−, in which the S atoms can adopt two different spin-orbit coupling positions: S2p$_{3/2}$ (164.1 eV) and S2p$_{1/2}$ (165.2 eV) [70,71], and 25% of −C−SO$_x$−C−, with x = 2 (167.5 eV), x = 3 (169.4 eV) or x = 4 (171.2 eV) [27]. This similar composition suggests that the assimilation mechanism of S species into the graphene structure is not affected by the presence of the other types of atoms.

The catalytic behaviour of the BNPS-Gr was studied by first measuring the cyclic voltammetry at a stationary disk electrode in both N_2- and O_2-saturated 0.1 M KOH solution (see Fig. 7a), which showed a clear reduction occurring at around −0.3 V in the O_2-saturated solution. Similar voltammograms were also obtained in O_2-saturated 0.1 M KOH solution at bare GC and graphene-modified (via drop-casting) GC electrodes in order to compare their performance with BNPS-Gr (Fig. 7b). It can be seen that the current density of the quaternary-doped graphene is much higher than that of graphene, which together with an earlier onset potential indicates that the addition of dopants into the graphene structure enhances the catalytic behaviour observed.

Next, the electrocatalytic activities of the quaternary-doped and single-doped graphenes were compared by rotating ring-disk electrode (RRDE) voltammetry for the ORR in O_2-saturated 0.1 M KOH electrolyte. Similar catalytic behaviour of all single-doped catalysts can be observed from the RRDE measurements at 1600 rpm (Fig. 7c), with an appreciably earlier onset potential for S-Gr of around + 0.02 V. In the

same figure, it can be seen that the quaternary-doped catalyst develops a greater catalytic activity with respect to the single-doped graphenes, showing the earliest onset potential and higher current density. These results are consistent with the Tafel analysis exhibited in Fig. 7d, where it can be seen that the Tafel slope of BNPS-Gr (93 mV dec^{-1}) is much lower than that of the single-doped graphenes, even being comparable to that calculated for commercial Pt/C (87 mV dec^{-1}).

The RRDE measurements for BNPS-Gr are displayed in Fig. 8a for rotation speeds from 400 to 2000 rpm. As expected, the ORR current density at the disk increases with increasing the rotation rate, in the same way that the formed peroxide is oxidized at the ring. From RRDE measurements of all catalysts the number of electrons involved in the ORR can be calculated using the Eq. (2) [72]:

$$ n = \frac{4I_D}{I_D + \left(\frac{I_R}{N}\right)} \tag{2} $$

where n is the number of electrons transferred, I_D the current measured at the GC disk ($I_D(H_2O) + I_D(H_2O_2)$), I_R the current measured at the Pt ring (related to the oxidation of H_2O_2) and N the collection efficiency (for the electrode used here, N = 0.37). Fig. 8b shows the values of n calculated with this method versus the potential applied at 1600 rpm. These values are quite stable in the range from −0.4 to −0.7 V, there being a similar result for B-Gr, N-Gr and S-Gr with a value of 3.2 at
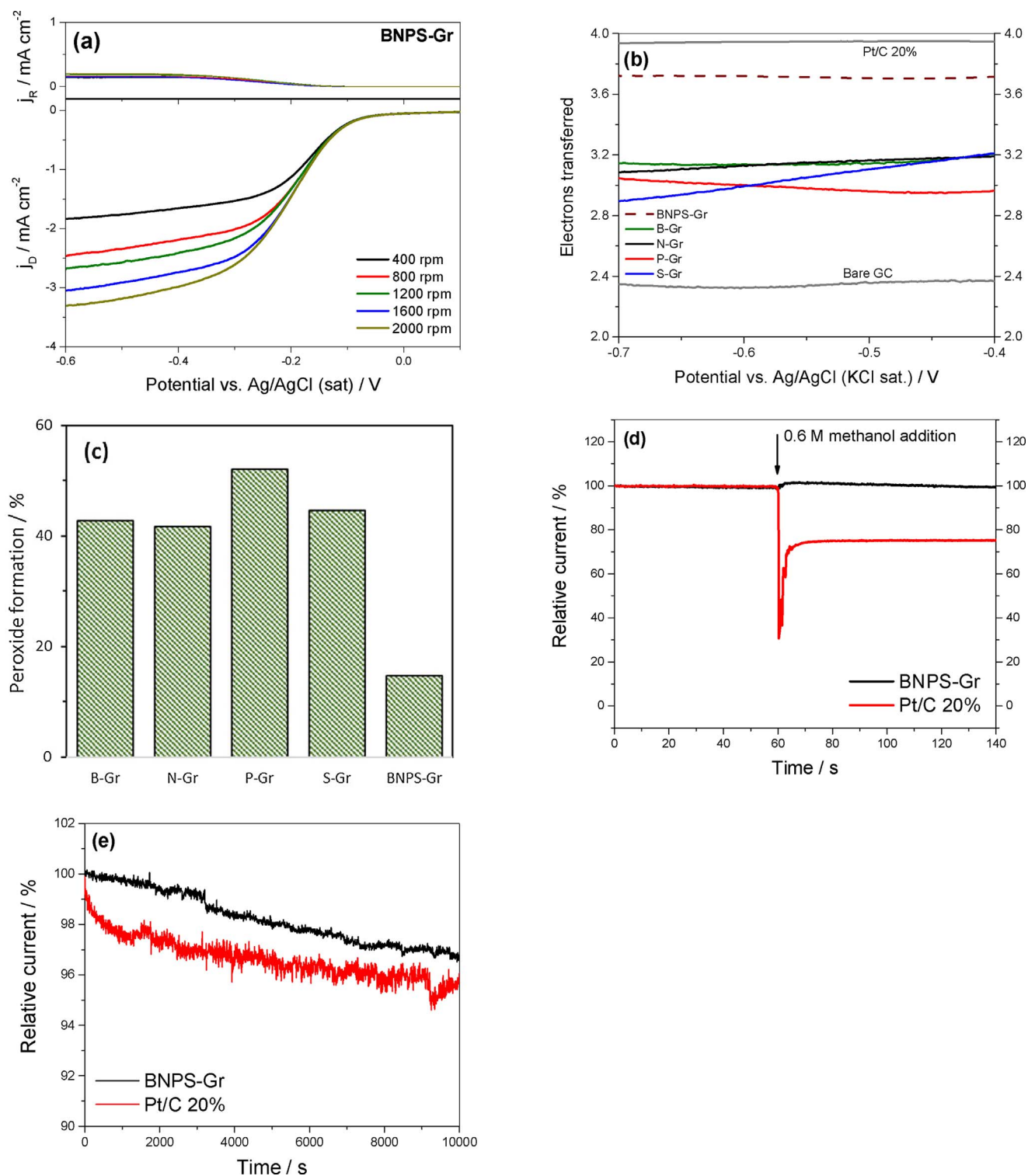
Fig. 8. (a) RRDE measurements of the quaternary-doped graphene at different rotation rates, showing the ring current density (j_R) at the top and disk current density (j_D) at the bottom. Ring potential is fixed at +0.5 V. (b) Number of electrons transferred during the ORR vs. the applied potential calculated from RRDE measurements at 1600 rpm using Eq (1). (c) Peroxide formed during the ORR at −0.5 V obtained from the values shown in (a). (d) Chronoamperometric responses at −0.5 V of BNPS-Gr and Pt/C 20% before and after the addition of 0.6 M methanol into the alkaline solution. (e) Durability test showing the chronoamperometric responses at −0.3 V of BNPS-Gr and Pt/C 20% in an O₂-saturated 0.1 M KOH solution at 1600 rpm.

−0.5 V, being slightly lower for P-Gr (3.0). In the other hand, n is considerably higher for the quaternary-doped catalyst with a value of 3.7, in accordance with the better catalytic behaviour observed in Fig. 7c. From the calculated values of n, the rates of peroxide formation are calculated and shown in Fig. 8c. The peroxide formation ranges between 41.7 and 52.0% for the single-doped graphene catalysts, there

being a considerable improvement for the BNPS-Gr catalyst with a peroxide production rate as low as 14.7%. This clearly illustrates the much higher efficiency of the quaternary-doped graphene towards the one-step ORR mechanism with respect the single-doped graphenes.

The improved catalytic activity exhibited by the quaternary-doped graphene versus the single-doped catalysts is unlikely to be mainly due

Table 3

Comparison of different dual- and ternary-doped graphene catalysts reported in the literature. *Values of potential converted from RHE into Ag/AgCl (sat. KCl): $E_{vs\ Ag/AgCl} = E_{vs\ RHE} - 0.197\ V - 0.059\ x\ pH$.

Catalyst	Cat. loading (mg cm^{-2})	E_{onset} (mV vs. Ag/AgCl)	j at -0.5 V (mA cm^{-2})	n at -0.5 V	Durability (remaining j after 10,000 s)	Ref.
BN-Gr*	0.204	-34	-3.15	3.5	86% (at -0.6 V, 1500 rpm)	[80]
PN-Gr*	0.5	-70	-3.80	3.5	97 % (at -0.3 V, 1600 rpm)	[81]
SN-Gr*	0.283	-44	-4.95	3.8	98 % (at -0.26 V, 1600 rpm)	[82]
BNP-Gr	0.6	-40	-4.10	3.5	91 % (at -0.3 V, 1600 rpm)	[49]
NPS-Gr*	0.503	-64	-4.95	3.3	93 % (at -0.26 V, 1600 rpm)	[74]
BNPS-Gr	**0.3**	**-30**	**-3.30**	**3.7**	**97 % (at -0.3 V, 1600 rpm)**	**–**

to improved electronic conductivity, since the Raman spectra (Fig. 4b) showed a very similar graphene 2D structure of BNPS-Gr with respect to N-Gr or B-Gr (noting that conductivity through a graphene layer is linked to the amount of defects present in its structure). According to some conclusions previously reported of carbon ternary-doped with heteroatoms, the simultaneous inclusion of different heteroatoms into the graphene structure can induce a synergistic effect with respect to their single-doped counterparts [73,74]. This is reportedly due to that the variability in the electronegativity of the different heteroatoms creates an asymmetry of the electronic charge density in the graphene lattice [47,48], thus increasing the adsorption of O_2 via the modulation of the π* bond of the O−O molecule [30]. Another feature that can have an impact on the ORR activity is the effect of the specific bonds formed between the heteroatoms and carbon during the annealing. In this case, the formation of P−N species in BNPS-Gr (Fig. 6c) has been reported to increase the number of active sites for O_2 adsorption [75]. Nevertheless, the B−N moieties (C-BNO and C-BN) created in the quaternary-doped catalyst (Fig. 6a) are believed to have a smaller contribution on the catalytic effect [76]. Analysis of the N1s (Fig. 6b) and S2p (Fig. 6d) features did not show significant differences between the BNPS-Gr and the single-doped catalysts.

The quaternary-doped catalyst was also tested and compared with respect to a commercial 20% Pt/C catalyst concerning their tolerance to the presence of methanol (see Fig. 8d), which can be an effect of the fuel crossover from the anode in methanol-fuelled fuel cells [77,78]. The chronoamperometric responses in an O_2-saturated 0.1 M KOH aqueous solution at fixed potential of -0.5 V and 1600 rpm electrode rotation speed are displayed in Fig. 7d before and after the addition of a certain amount of methanol for a final composition of 0.6 M. It is observed an immediate decrease of 25% on the response in the case of Pt/C due to the poisoning effect of the CO intermediates on the Pt catalyst [79]. On the other hand, the BNPS-Gr is not affected by the presence of methanol. This points to the high selectivity of the quaternary-doped catalyst towards the ORR, which makes BNPS-Gr a promising catalyst for its application in methanol-fuelled fuel cells.

Another important feature in catalysis is the stability of a catalyst under continuous operation. A durability test was performed at a fixed potential of -0.3 V in O_2-saturated 0.1 M KOH solution for the quaternary-doped graphene catalyst and a commercial Pt/C 20% (see Fig. 8e). A decrease of around 3% was observed in the measured current density for the BNPS-Gr catalyst after 10 000 s of continuous operation, which is lower than that observed for the commercial Pt/C 20% under the same conditions. This reflects the higher stability of this graphene-derived catalyst with respect to Pt-catalysts under strongly alkaline conditions, which highlights the potential of the catalyst presented in this work for practical fuel cell applications.

Finally, in order to provide a complete picture on doped-graphene catalysis, Table 3 shows illustrative results obtained from the literature of some dual- and ternary-doped graphene catalysts compared to the presently reported quaternary-doped graphene. Although it is important to be cautious when comparing catalysts reported from different papers due to the high variability in the conditions of synthesis and evaluation, it can be seen that BNPS-Gr shows excellent values of onset potential, number of electrons transferred during ORR and

durability. Nevertheless, it is reported a lower catalytic activity in terms of current density for the quaternary catalyst, although it should be noted that those dual and ternary-doped graphenes reporting higher values of j where tested with catalyst loadings of almost the double with respect the BNPS-Gr (except the SN-Gr). In conclusion, this comparison highlights the importance of the presently reported quaternary-doped graphene in the framework of metal-free doped-graphene catalysis for the ORR.

4. Conclusions

A novel metal-free catalyst based on graphene doped with B, N, P and S is reported. XRD measurements show the efficiency of the thermal treatment turning the GO structure of the precursor into graphene configuration. The Raman spectroscopy demonstrated that the presence of defects into the graphene layers is closely related to the size of the dopant atoms, B and N dopants producing fewer defects in the structure than P and S. The composition and the nature of the carbon-heteroatom bonding was determined by XPS, suggesting that the B−N and P−N bonds (mainly the latter) reflected in B1s and P2p spectra of BNPS-Gr could have a positive impact in the catalytic activity. In this regard, the quaternary-doped catalyst developed a better ORR performance than the single-doped catalysts, attributed to the different electronegativity values of the several dopants which supposedly can modulate the O_2 molecule binding energy facilitating its dissociation. Finally, comparative tests of methanol tolerance concluded that a commercial Pt/C catalyst suffers a 25% of performance decrease in presence of a 0.6 M methanol solution, whereas the BNPS-Gr is not affected by the methanol. These results suggest that the novel quaternary-doped graphene catalyst is a promising alternative to current Pt and transition-metal catalysts for energy applications, with special attention to methanol-fuelled fuel cells.

References

[1] S. Stankovich, D.A. Dikin, G.H.B. Dommett, K.M. Kohlhaas, E.J. Zimney, E.A. Stach, R.D. Piner, S.T. Nguyen, R.S. Ruoff, Nature 442 (2006) 282–286.
[2] K.S. Novoselov, V.I. Fal'ko, L. Colombo, P.R. Gellert, M.G. Schwab, K. Kim, Nature 490 (2012) 192–200.
[3] A. Marinkas, F. Arena, J. Mitzel, G.M. Prinz, A. Heinzel, V. Peinecke, H. Natter, Carbon N. Y. 58 (2013) 139–150.
[4] S.K. Bikkarolla, P. Cumpson, P. Joseph, P. Papakonstantinou, Faraday Discuss. 173 (2014) 415–428.
[5] Y. Jiao, Y. Zheng, M. Jaroniec, S.Z. Qiao, J. Am. Chem. Soc. 136 (2014) 4394–4403.

[6] Y. Sha, T.H. Yu, B.V. Merinov, P. Shirvanian, W.A. Goddard, J. Phys. Chem. C 116 (2012) 21334–21342.

[7] K. Shimizu, L. Sepunaru, R.G. Compton, Chem. Sci. 7 (2016) 3364–3369.

[8] C. Huang, C.-L. Li, G. Shi, Energy Environ. Sci. 5 (2012) 8848–8868.

[9] X.-K. Kong, C.-L. Chen, Q.-W. Chen, Chem. Soc. Rev. 43 (2014) 2841–2857.

[10] X. Li, H. Wang, J.T. Robinson, H. Sanchez, G. Diankov, H. Dai, J. Am. Chem. Soc. 131 (2009) 15939–15944.

[11] L. Qu, Y. Liu, J.-B. Baek, L. Dai, ACS Nano 4 (2010) 1321–1326.

[12] D. Higgins, Z. Chen, D.U. Lee, Z. Chen, J. Mater. Chem. A 1 (2013) 2639–2645.

[13] T.N. Huan, T. Van Khai, Y. Kang, K.B. Shim, H. Chung, J. Mater. Chem. 22 (2012) 14756–14762.

[14] L. Lai, J.R. Potts, D. Zhan, L. Wang, C.K. Poh, C. Tang, H. Gong, Z. Shen, J. Lin, R.S. Ruoff, Energy Environ. Sci. 5 (2012) 7936–7942.

[15] H. Wang, M. Xie, L. Thia, A. Fisher, X. Wang, J. Phys. Chem. Lett. 5 (2014) 119–125.

[16] R. Vishwakarma, G. Kalita, S.M. Shinde, Y. Yaakob, C. Takahashi, M. Tanemura, Mater. Lett. 177 (2016) 89–93.

[17] Y.A. Kim, K. Fujisawa, H. Muramatsu, T. Hayashi, M. Endo, T. Fujimori, K. Kaneko, M. Terrones, J. Behrends, A. Eckmann, C. Casiraghi, K.S. Novoselov, R. Saito, M.S. Dresselhaus, ACS Nano 6 (2012) 6293–6300.

[18] D.-Y. Yeom, W. Jeon, N.D.K. Tu, S.Y. Yeo, S.-S. Lee, B.J. Sung, H. Chang, J.A. Lim, H. Kim, Sci. Rep. 5 (2015) 9817.

[19] S. Agnoli, M. Favaro, J. Mater. Chem. A 4 (2016) 5002–5025.

[20] L. Niu, Z. Li, W. Hong, J. Sun, Z. Wang, L. Ma, J. Wang, S. Yang, Electrochim. Acta 108 (2013) 666–673.

[21] V. Thirumal, A. Pandurangan, R. Jayavel, R. Ilangovan, Synth. Met. 220 (2016) 524–532.

[22] Z.W. Liu, F. Peng, H.J. Wang, H. Yu, W.X. Zheng, J. Yang, Angew. Chem.—Int. Ed. 50 (2011) 3257–3261.

[23] C. Zhang, N. Mahmood, H. Yin, F. Liu, Y. Hou, Adv. Mater. 25 (2013) 4932–4937.

[24] J. Wu, C. Jin, Z. Yang, J. Tian, R. Yang, Carbon N. Y. 82 (2015) 562–571.

[25] L. Zhang, J. Niu, M. Li, Z. Xia, J. Phys. Chem. C 118 (2014) 3545–3553.

[26] M. Klingele, C. Pham, K.R. Vuyyuru, B. Britton, S. Holdcroft, A. Fischer, S. Thiele, Electrochem. Commun. 77 (2017) 71–75.

[27] Z. Yang, Z. Yao, G. Li, G. Fang, H. Nie, Z. Liu, X. Zhou, X. Chen, S. Huang, ACS Nano 6 (2012) 205–211.

[28] Z. Ma, S. Dou, A. Shen, L. Tao, L. Dai, S. Wang, Angew. Chem.—Int. Ed. 54 (2015) 1888–1892.

[29] F. Razmjooei, K.P. Singh, D.-S. Yang, W. Cui, Y.H. Jang, J.-S. Yu, ACS Catal. 7 (2017) 2381–2391.

[30] X. Ge, A. Sumboja, D. Wuu, T. An, B. Li, F.W.T. Goh, T.S.A. Hor, Y. Zong, Z. Liu, ACS Catal. 5 (2015) 4643–4667.

[31] E.H. Yu, X. Wang, U. Krewer, L. Li, K. Scott, Energy Environ. Sci. 5 (2012) 5668.

[32] X. Wang, G. Sun, P. Routh, D.-H. Kim, W. Huang, P. Chen, Chem. Soc. Rev. 43 (2014) 7067–7098.

[33] H. Zhao, K.S. Hui, K.N. Hui, Carbon N. Y. 76 (2014) 1–9.

[34] Z.-H. Sheng, H.-L. Gao, W.-J. Bao, F.-B. Wang, X.-H. Xia, J. Mater. Chem. 22 (2012) 390–395.

[35] L. Zhang, Z. Xia, J. Phys. Chem. C 115 (2011) 11170–11176.

[36] D.S. Yang, D. Bhattacharjya, S. Inamdar, J. Park, J.S. Yu, J. Am. Chem. Soc. 134 (2012) 16127–16130.

[37] Y. Zhang, K. Fugane, T. Mori, L. Niu, J. Ye, J. Mater. Chem. 22 (2012) 6575–6580.

[38] S. Wang, L. Zhang, Z. Xia, A. Roy, D.W. Chang, J.B. Baek, L. Dai, Angew. Chem.—Int. Ed. 51 (2012) 4209–4212.

[39] J. Liang, Y. Jiao, M. Jaroniec, S.Z. Qiao, Angew. Chem.—Int. Ed. 51 (2012) 11496–11500.

[40] C. Zhang, X. Wang, Q. Liang, X. Liu, Q. Weng, J. Liu, Y. Yang, Z. Dai, K. Ding, Y. Bando, J. Tang, D. Golberg, Nano Lett. 16 (2012) 2054–2060.

[41] G. Jo, J. Sanetuntikul, S. Shanmugam, RSC Adv. 5 (2015) 53637–53643.

[42] C. Huang, L. Han, L. Wu, R. Su, J. Chen, P. Lu, Eur. Phys. J. B 88 (2015) 1–7.

[43] X. Yu, Y. Kang, H.S. Park, Carbon N. Y. 101 (2016) 49–56.

[44] C.H. Choi, S.H. Park, S.I. Woo, ACS Nano 6 (2012) 7084–7091.

[45] Z. Guo, Z. Xiao, G. Ren, G. Xiao, Y. Zhu, L. Dai, L. Jiang, Nano Res. 9 (2016) 1244–1255.

[46] J. Zhang, L. Dai, Angew. Chem.—Int. Ed. 55 (2016) 13296–13300.

[47] C.H. Choi, M.W. Chung, S.H. Park, S.I. Woo, Phys. Chem. Chem. Phys. 15 (2013) 1802–1805.

[48] S. Zhao, J. Liu, C. Li, W. Ji, M. Yang, H. Huang, Y. Liu, Z. Kang, ACS Appl. Mater. Interfaces 6 (2014) 22297–22304.

[49] H. Lin, L. Chu, X. Wang, Z. Yao, F. Liu, Y. Ai, X. Zhuang, S. Han, New J. Chem. 40 (2016) 6022–6029.

[50] Z. Guo, G. Ren, C. Jiang, X. Lu, Y. Zhu, L. Jiang, L. Dai, Sci. Rep. 5 (2015) 17064.

[51] J. Zhang, Z. Zhao, Z. Xia, L. Dai, Nat. Nanotechnol. 10 (2015) 444–452.

[52] Y. Garsany, I.L. Singer, K.E. Swider-Lyons, J. Electroanal. Chem. 662 (2011) 396–406.

[53] Y. Su, Y. Zhang, X. Zhuang, S. Li, D. Wu, F. Zhang, X. Feng, Carbon N. Y. 62 (2013) 296–301.

[54] L. Sun, L. Wang, C. Tian, T. Tan, Y. Xie, K. Shi, M. Li, H. Fu, RSC Adv. 2 (2012) 4498–4506.

[55] M. Khalfaoui, S. Knani, M.A. Hachicha, A. Ben Lamine, J. Colloid Interface Sci. 263 (2003) 350–356.

[56] Z. Sheng, L. Shao, J. Chen, W. Bao, F. Wang, X. Xia, ACS Nano 5 (2011) 4350–4358.

[57] C. Liang, Z. Li, S. Dai, Angew. Chem.—Int. Ed. 47 (2008) 3696–3717.

[58] C. Yu, Z. Liu, X. Meng, B. Lu, D. Cui, J. Qiu, Nanoscale 8 (2016) 17458–17464.

[59] Y. Li, J. Yang, J. Huang, Y. Zhou, K. Xu, N. Zhao, X. Cheng, Carbon N. Y. 122 (2017) 237–246.

[60] A.C. Ferrari, J. Robertson, Phys. Rev. B 61 (2000) 14095–14107.

[61] Y. Li, J. Yang, N. Zhao, J. Huang, Y. Zhou, K. Xu, N. Zhao, Appl. Catal. A: Gen. 534 (2017) 30–39.

[62] P. Mallet-Ladeira, P. Puech, C. Toulouse, M. Cazayous, N. Ratel-Ramond, P. Weisbecker, G.L. Vignoles, M. Monthioux, Carbon N. Y. 80 (2014) 629–639.

[63] Z. Jiang, X. Zhao, X. Tian, L. Luo, J. Fang, H. Gao, Z.J. Jiang, ACS Appl. Mater. Interfaces 7 (2015) 19398–19407.

[64] X. Zhao, Q. Zhang, B. Zhang, C.-M. Chen, A. Wang, T. Zhang, D.S. Su, J. Mater. Chem. 22 (2012) 4963–4969.

[65] S. Hou, X. Cai, H. Wu, X. Yu, M. Peng, K. Yan, D. Zou, Energy Environ. Sci. 6 (2013) 3356–3362.

[66] M. Chisaka, T. Iijima, Y. Ishihara, Y. Suzuki, R. Inada, Y. Sakurai, Electrochim. Acta 85 (2012) 399–410.

[67] J.P. Paraknowitsch, Y. Zhang, B. Wienert, A. Thomas, Chem. Commun. 49 (2013) 1208–1210.

[68] O. El Zubir, I. Barlow, G.J. Leggett, N.H. Williams, Nanoscale 5 (2013) 11125–11131.

[69] F. Razmjooei, K.P. Singh, M.Y. Song, J.S. Yu, Carbon N. Y. 78 (2014) 257–267.

[70] C. Chen, W. Fan, Q. Zhang, X. Fu, H. Wu, Ionics (Kiel) 21 (2015) 3233–3238.

[71] H. Zhang, X. Liu, G. He, X. Zhang, S. Bao, W. Hu, J. Power Sources 279 (2015) 252–258.

[72] E. Claude, T. Addou, J. Latour, P. Aldebert, J. Appl. Electrochem. 28 (1998) 57–64.

[73] J.-S. Li, S.-L. Li, Y.-J. Tang, K. Li, L. Zhou, N. Kong, Y.-Q. Lan, J.-C. Bao, Z.-H. Dai, Sci. Rep. 4 (2015) 5130.

[74] J. Wu, X. Zheng, C. Jin, J. Tian, R. Yang, Carbon N. Y. 92 (2015) 327–338.

[75] R. Li, Z. Wei, X. Gou, ACS Catal. 5 (2015) 4133–4142.

[76] Y. Zhao, L. Yang, S. Chen, X. Wang, Y. Ma, Q. Wu, Y. Jiang, W. Qian, Z. Hu, J. Am. Chem. Soc. 135 (2013) 1201–1204.

[77] A. Heinzel, V.M. Barragán, J. Power Sources 84 (1999) 70–74.

[78] K. Scott, W. Taama, P. Argyropoulos, K. Sundmacher, J. Power Sources 83 (1999) 204–216.

[79] D.Y. Chung, D. Kim, Y.-H. Chung, M.J. Lee, S.J. Yoo, A.D. Bokare, W. Choi, Y.-E. Sung, Sci. Rep. 4 (2014) 7450.

[80] I.T. Kim, M.J. Song, Y.B. Kim, M.W. Shin, Int. J. Hydrogen Energy 41 (2016) 22026–22033.

[81] X. Qiao, S. Liao, C. You, R. Chen, Catalysts 5 (2015) 981–991.

[82] F. Pan, Y. Duan, X. Zhang, J. Zhang, ChemCatChem 8 (2016) 163–170.